Exceptional precision of a nonlinear optical sensor at a square-root singularity

K. J. H. Peters[1] and S. R. K. Rodriguez[1,*]

[1] *Center for Nanophotonics, AMOLF, Science Park 104, 1098 XG Amsterdam, The Netherlands*

(Dated: June 6, 2022)

Exceptional points (EPs) — spectral singularities of non-Hermitian linear systems — have recently attracted interest for sensing. While initial proposals and experiments focused on enhanced sensitivities neglecting noise, subsequent studies revealed issues with EP sensors in noisy environments. Here we propose a single-mode Kerr-nonlinear resonator for exceptional sensing in noisy environments. Based on the resonator's dynamic hysteresis, we define a signal that displays a square-root singularity reminiscent of an EP. However, our sensor has crucial fundamental and practical advantages over EP sensors: the signal-to-noise ratio increases with the measurement speed, the square-root singularity is easily detected through intensity measurements, and both sensing precision and information content of the signal are enhanced around the singularity. Our sensor also overcomes the fundamental trade-off between precision and averaging time characterizing all linear sensors. All these unconventional features open up new opportunities for fast and precise sensing using hysteretic resonators.

In 2014, Wiersig proposed using a non-Hermitian degeneracy known as an exceptional point (EP) for sensing [1]. An EP occurs when a pair of eigenvalues and eigenvectors of a non-Hermitian Hamiltonian coalesce. Two coupled linear resonators constitute the typical system where EPs have been observed [2–10] and used for sensing [11–14]. Setting $\hbar = 1$, the coupled resonators are described by a 2×2 Hamiltonian with complex frequencies $\tilde{\omega}_j$ $(j = 1, 2)$ in the diagonal and coupling constant g in the off-diagonal. The Hamiltonian's eigenvalues are

$$\omega_\pm = \tilde{\omega}_{av} \pm \frac{\tilde{\Delta}}{2}\sqrt{1 + \left(\frac{2g}{\tilde{\Delta}}\right)^2}, \tag{1}$$

with $\tilde{\omega}_{av} = (\tilde{\omega}_1 + \tilde{\omega}_2)/2$ the average complex frequency and $\tilde{\Delta} = \tilde{\omega}_1 - \tilde{\omega}_2$ the complex detuning [15]. Notice the square-root singularity for $2g/\tilde{\Delta} = \pm i$, where the eigenvalues ω_+ and ω_- coalesce; this is the EP. At the EP, a perturbation to a resonance frequency [i.e., $\Re[\tilde{\omega}_j] \to \Re[\tilde{\omega}_j] + \epsilon$ $(j = 1$ or $2)$] results in a splitting $\Re[\omega_+ - \omega_-] \propto \sqrt{\epsilon}$. Essentially, Wiersig proposed using this frequency splitting and the associated linewidth splitting $\Im[\omega_+ - \omega_-]$ as signals for sensing. Unlike conventional sensors where signals scale linearly with ϵ [16–22], the $\sqrt{\epsilon}$ scaling near an EP promised greater sensitivities for small ϵ [1].

Wiersig's proposal met great enthusiasm and skepticism recently. On one hand, experimental claims of enhanced sensitivities [11–13] and proposed applications [14, 23–31] of EP sensors have generated excitement [32, 33]. On the other hand, it has been argued that the precision of EP sensors is degraded by noise [34–36]. The observation of enhanced fluctuations near an EP supports this criticism [37]. The foregoing debate reveals that the sensitivity, i.e., scaling of signal with perturbation, is insufficient to characterize sensing performance. Particularly important are the effects of noise, which ultimately determine the magnitude of the perturbation that can be detected within a certain measurement time.

In this Letter we propose and numerically demonstrate optical sensing beyond the constraints of linear sensors using a single coherently-driven Kerr-nonlinear resonator. We propose to measure the splitting in transmitted intensities at the endpoints of a hysteresis cycle. This intensity splitting scales with the square root of the perturbation strength. Remarkably, the sensing precision and information content of the signal are enhanced around the square-root singularity. Our sensor also exhibits a signal-to-noise ratio that increases with the measurement speed, and an anomalous scaling of the precision with the averaging time. Crucial for practical applications, our approach only requires monochromatic intensity measurements, and avoids the cumbersome and error-prone task of fitting spectral lineshapes to extract complex eigenvalues (as done in EP sensors).

Our sensor can be realized using Fabry-Pérot [38–47], whispering-gallery-mode [17, 18, 21, 22, 48], ring [49–51], photonic crystal [52–57] or any cavity architecture where one mode is spectrally distant from all other modes and probes an intensity-dependent refractive index. In a frame rotating at the driving frequency ω, the intracavity field α satisfies

$$i\dot{\alpha}(t) = \left[-\Delta - \frac{i\Gamma}{2} + U(|\alpha(t)|^2 - 1)\right]\alpha(t) + i\sqrt{\kappa_L}F + D\xi(t). \tag{2}$$

$\Delta = \omega - \omega_0$ is the laser's detuning from the resonance frequency ω_0. The total loss rate $\Gamma = \gamma + \kappa_L + \kappa_R$ includes intrinsic loss at rate γ and leakage through 'left' and 'right' input-output ports at rates κ_L and κ_R. U is the Kerr nonlinearity strength. $D\xi(t) = D[\xi_1(t) + i\xi_2(t)]/\sqrt{2}$ represents Gaussian white noise with variance D^2 in the field quadratures. $\xi_j(t)$ have zero mean $[\langle\xi_j(t)\rangle = 0]$ and correlation $\langle\xi_j(t)\xi_k(t + t')\rangle = \delta_{j,k}\delta(t')$. The validity of Eq. 2 for $U \ll \Gamma$ (henceforth assumed) has been verified many times, through quantitative agreement with experiments and full quantum calculations [58].

As usual in optical sensing [17, 18, 21, 22, 40, 42, 45,

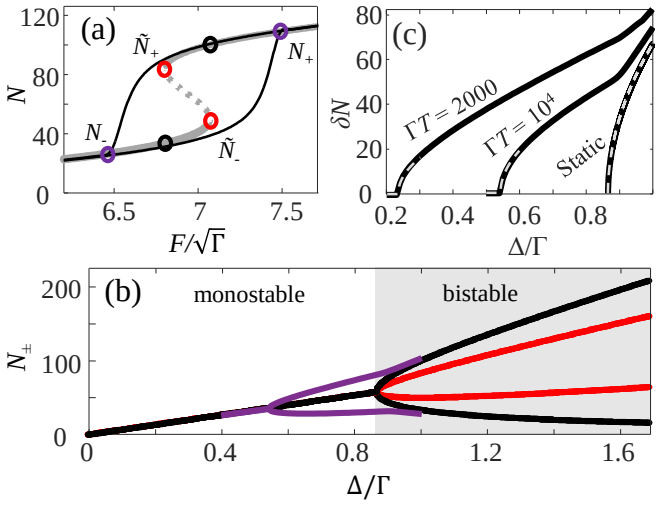

FIG. 1. (a) Intracavity photon number N versus driving amplitude F referenced to the loss rate Γ. The laser-cavity detuning is $\Delta = \Gamma$, and there is no noise. Gray solid and dotted curves represent stable and unstable steady states, respectively. Thin black curves represent the dynamic hysteresis obtained by linearly scanning $F/\sqrt{\Gamma}$ from 0 to 10 and back within a time $T = 10^4/\Gamma$. Red open circles indicate the turning points $\tilde{N}_\pm$. Purple open circles indicate the crossing points $N_\pm$ for the dynamic case, which are used in Figs. 2 and 3 as a signal for sensing. Black open circles indicate $N_\pm$ in the adiabatic limit $\Gamma T \to \infty$. Inset: schematic of the proposed sensor, i.e. a Kerr-nonlinear resonator. (b) Red curves are the turning points $\tilde{N}_\pm$, and black curves are the crossing points $N_\pm$, both in the adiabatic limit. $N_\pm$ in the dynamic case are shown in purple. Parameter values: $\Gamma = 1$, $\gamma = \Gamma/6$, $\kappa_L = \Gamma/2$, $\kappa_R = \Gamma/3$, $U = \Gamma/100$. (c) Solid curves represent the splitting $\delta N = N_+ - N_-$ proposed as a signal for sensing, as function of Δ/Γ. Two curves correspond to scans $F(t)$ within different time T, and the other curve corresponds to the adiabatic limit. Dashed lines are square-root fits as explained in the text.

48], our goal is to detect a perturbation ϵ to ω_0. For this purpose, we define the signal in a way that is inspired (but not restricted) by the behavior of the steady-state solutions to Eq. 2 ($\dot{\alpha} = D = 0$) near the onset of bistability. There, two stable states with different intra-cavity intensity $N = |\alpha|^2$ exist at a single driving condition. Figure 1(a) shows bistability for $\Delta = \Gamma$ and variable $F/\sqrt{\Gamma}$. Solid and dotted gray curves are stable and unstable steady states, respectively. The bistability range is bound by the turning points $\tilde{N}_\pm$ [red circles in Fig. 1(a)], obtained by setting $d|F|^2/dN = 0$ in Eq. 2:

$$\tilde{N}_\pm = \frac{2\Delta}{3U} \pm \frac{2\Delta}{6U}\sqrt{1 - \left(\frac{\sqrt{3}\Gamma}{2\Delta}\right)^2}. \qquad (3)$$

Notice the resemblance to Eq. 1: $\tilde{N}_\pm$ are defined by a square-root function with singularity at the critical detuning $\Delta_c = \sqrt{3}\Gamma/2$. $\tilde{N}_\pm$ coalesce at Δ_c, just like $\omega_\pm$ coalesce at the EP. This suggests using $\tilde{N}_+ - \tilde{N}_-$ as signal for sensing. However, $\tilde{N}_\pm$ are steady-state solutions expected in quasi-static protocols only. Fast protocols display no sharp turns in N thereby making $\tilde{N}_\pm$ ill-defined. This is illustrated by the thin black curves in Fig. 1(a), obtained by scanning $F/\sqrt{\Gamma}$ from 0 to 10 and back within a time $T = 10^4/\Gamma$. Clearly, $\tilde{N}_\pm$ cannot be used for fast sensing. We therefore turn our attention to the crossing points $N_\pm$, where upwards and downwards scans intersect. $N_\pm$ are marked in Fig. 1(a) by purple (black) circles for the dynamic (static) case.

Figure 1(b) compares the crossing points $N_\pm$ to the turning points $\tilde{N}_\pm$ as Δ (and hence ϵ) varies. For adiabatic protocols following the steady-state solutions, $N_\pm$ (black curves) and $\tilde{N}_\pm$ (red curves) both bifurcate at Δ_c. However, $N_\pm$ offer greater sensitivity in adiabatic protocols since $N_+ - N_- \geq \tilde{N}_+ - \tilde{N}_-$. More importantly, $N_\pm$ are well defined and display the desired square-root scaling even for non-adiabatic protocols. At high speeds the square-root singularity lies below Δ_c, where there is no bistability or static hysteresis; see where the purple curve bifurcates in Fig. 1(b). Nonetheless, dynamic hysteresis still emerges [43, 59], and the intensity splitting $\delta N = N_+ - N_-$ can be unambiguously defined as signal for fast sensing. Practically, δN is determined by measuring the time-dependent intensities N_f and N_b when ramping F forward and backward, respectively. N_+ and N_- are then the first values of N at which $N_b - N_f = 0$ when F increases and decreases, starting from the center of the hysteresis where $N_b - N_f$ is maximum.

Figure 1(c) shows how δN scales with Δ/Γ for two non-adiabatic protocols, one with period $T = 2000/\Gamma$ and another with $T = 10^4/\Gamma$. The static δN, corresponding to $T \to \infty$, is shown for reference. All δN are fitted (see dashed gray curves) with square-root functions near the singularity at Δ_{SS}; this is the point where N_+ and N_- coalesce. The excellent fits evidence that the desired square-root scaling persists for detunings below the static bistability threshold Δ_c and for highly non-adiabatic protocols. Actually, our approach works for any positive detuning, but $\Delta < \Delta_c$ is advantageous for fast sensing because Δ_{SS} decreases with speed as Fig. 1(c) shows. However, there is a trade-off between measurement speed and sensitivity: faster protocols decrease the pre-factor in the square-root scaling of δN with Δ. In supplemental material (SM) we quantify this trade-off and discuss the role of model parameters in general [60].

Next we assess the effects of noise by numerically solving Eq. 2 using the xSPDE MATLAB toolbox [62]. Equation 2 only contains additive noise $\xi(t)$, representing fluctuations in the laser's amplitude & phase and dissipation-induced fluctuations of the intra-cavity field; the effect of detuning noise is discussed in SM [60]. We consider a single hysteresis cycle of duration T, which also determines the measurement time. Figure 2(a) shows the crossing points $N_\pm$ comprising δN, and the standard deviation $\sigma_{\delta N}$ of δN, both as a function of ΓT. The calculations

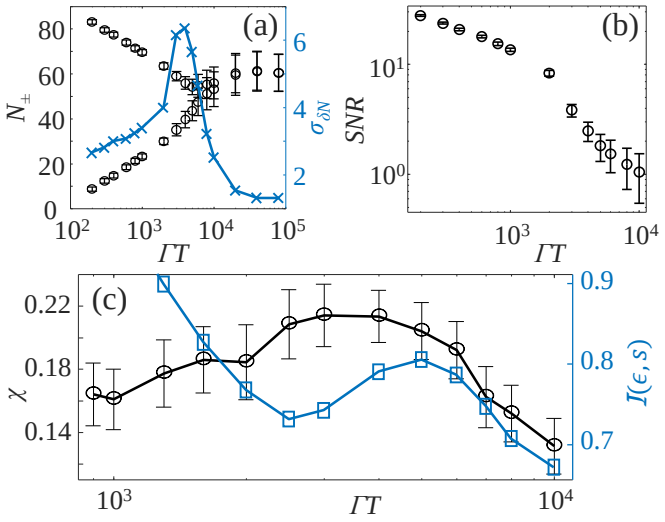

FIG. 2. (a) Black circles are the crossing points $N_\pm$ comprising the signal $\delta N = N_+ - N_-$. Blue crosses are the standard deviation of δN, i.e. $\sigma_{\delta N}$. Both δN and $\sigma_{\delta N}$ are show for variable ramp time T referenced to Γ. (b) Signal-to-noise ratio $\delta N/\sigma_{\delta N}$ versus ΓT. (c) Precision figure of merit χ versus ΓT. Parameters are as in Fig. 1, with $\Delta/\Gamma = 0.7$ and $D/F_{\rm avg} = 1/50$. Each point in (a,b) is calculated based on 1200 individual cycles with different noise realizations. Error bars indicate one standard deviation of the mean. Errors in (c) are based on 10 calculations of χ, each calculation involving 1200 noise realizations.

are done for fixed $\Delta = 0.7\Gamma$ and $D/F_{\rm avg} = 1/50$, with $F_{\rm avg}$ the average driving amplitude. $\sigma_{\delta N}$ is obtained by calculating δN for 1200 different noise realizations.

Figure 2(a) shows that N_+ and N_- are approximately equal for large ΓT. Indeed, there is no hysteresis in the adiabatic limit for the selected $\Delta = 0.7\Gamma$. Therefore, contrary to conventional sensors, our sensor's performance can be enhanced by reducing the measurement time T. The signal $\delta N = N_+ - N_-$ only becomes appreciable below a critical time $T_{\rm SS}$, where the system crosses the square-root singularity. This way of approaching a square-root singularity (by varying the ramp time) is advantageous over the usual approach in EP sensors, where the detuning and/or the losses of the resonators [2, 5, 6, 8, 10] are slowly varied. Our approach can be orders of magnitude faster thanks to the availability of high-frequency amplitude modulators.

Figure 2(a) also shows how the fluctuations in δN scale with T. The peak in $\sigma_{\delta N}$ at $\Gamma T \approx 4 \times 10^3$ evidences enhanced fluctuations around the square-root singularity. This peak is reminiscent of the enhanced fluctuations at an EP [37], which are at the heart of the aforementioned debate [34–36, 63]. While this effect seems discouraging, our statistical analysis below proves that a sensing advantage remains at the square-root singularity.

Figure 2(b) shows the signal-to-noise ratio $SNR = \delta N/\sigma_{\delta N}$, following a double power law decay with ΓT. The transition between power laws occurs around $T_{\rm SS}$, where signal fluctuations are enhanced. The SNR follows a similar scaling with ΓT as the dynamic hysteresis area [43, 64], resulting in stronger signals at high speeds. However, the laser power needed to cross the full hysteresis range (and hence to measure the signal) also increases with the speed [64]. Hence, there is a trade-off between energy consumption and measurement speed.

Figures 2(a,b) suggest that, if detection speed is most important and power is available, the cycle time T should be reduced as much as possible and thereby disregard the square-root singularity location. However, for many sensors, precision is also important. A precise measurement is one in which the mean change in the signal due to the perturbation is large compared to the uncertainty in that measurement. In this vein, we define $\chi = (\overline{\delta N}_\epsilon - \overline{\delta N}_0)/(\sigma_0 + \sigma_\epsilon)$ to quantify the precision. $\overline{\delta N}_\epsilon$ and $\overline{\delta N}_0$ are the mean splitting measured for the perturbed and unperturbed cavity, respectively. σ_0 and σ_ϵ are standard deviations corresponding to those signals. Thus, χ quantifies the mean change in the signal relative to the measurement uncertainty.

Figure 2(c) shows χ versus ΓT. For each T, we performed 12×10^3 simulations with different realizations of the noise for a perturbed ($\epsilon = \Gamma/100$) and an unperturbed cavity. We then calculated χ based on the means and standard deviations of the distributions of signals measured for the two cavities. Interestingly, the peak in χ approximately coincides with $T_{\rm SS}$, thereby demonstrating the precision enhancement by the square-root singularity. While χ remains below one (a commonly used detection threshold) in Fig. 2(c), a reliable detection strategy can still be constructed for small χ by allowing a greater probability of missed detection [65]. Overall, Fig. 2(c) reveals a trade-off between measurement time (defined by T) and precision. If precision matters most, one should modulate F with period $T \approx T_{\rm SS}$. However, if speed is crucial, $T < T_{\rm SS}$ can be selected.

In SM we show that our nonlinear sensor can compete or outperform a linear sensor in certain parameter regimes [60]. For the comparison, we took equal dissipation, noise strength, detuning, and average driving power. However, a direct comparison is impossible for two reasons mainly. First, our sensor's performance depends on the parameter U, absent in linear sensors. Second, for linear resonators the SNR increases with power, but for our sensor mainly the cycle time T determines the SNR. Despite these differences, our results demonstrate that our sensing strategy can compete with linear sensors. Crucially, our claim does not rely on static sensitivities only, and our approach embraces nonlinearities which typically degrade the precision of linear sensors.

Next we asses our sensor's performance using information theory. We are interested in the mutual information between a perturbation ϵ and its induced signal shift $\mathcal{S} = \delta N_\epsilon - \overline{\delta N}_0$, given by

$$\mathcal{I}(\epsilon;\mathcal{S}) = \sum_{s\in S}\sum_{\varepsilon\in E} p_{(\epsilon,\mathcal{S})}(\varepsilon,s)\log\frac{p_{(\epsilon,\mathcal{S})}(\varepsilon,s)}{p_\epsilon(\varepsilon)p_\mathcal{S}(s)}. \quad (4)$$

$p_\epsilon(\varepsilon)$ and $p_\mathcal{S}(s)$ are marginal distributions representing our uncertainty in the perturbation and signal, respectively, and $p_{(\epsilon,\mathcal{S})}(\varepsilon,s)$ is their joint probability distribution. $\mathcal{I}(\epsilon;\mathcal{S})$ quantifies the information ϵ and $\mathcal{S}$ share, or how much knowledge of $\mathcal{S}$ reduces uncertainty of ϵ [66].

We model our uncertainty in the perturbation by defining $p_\epsilon(\varepsilon)$ as a Gaussian distribution with mean $\Gamma/100$ and standard deviation $\Gamma/1000$. Then, we determine $p_\mathcal{S}(s)$ by numerically calculating $\mathcal{S}$ using 1200 different noise seeds for each cycle time ΓT. This involves calculating δN for the unperturbed (detuning Δ_0) and perturbed ($\Delta_\epsilon = \Delta_0 + \epsilon$) cavity, with $\Delta_0 = 0.7\Gamma$ and ϵ drawn from $p_\epsilon(\varepsilon)$. Finally, we determine $p_{(\epsilon,\mathcal{S})}(\varepsilon,s)$ based on the value of $\mathcal{S}$ for each member of $p_\epsilon(\varepsilon)$.

Figure 2(c) shows that $\mathcal{I}$ is a non-monotonic function of ΓT. For small ΓT, $\mathcal{I}$ increases with decreasing ΓT; this is expected based on the growing SNR as shown in Fig. 2(b). For large ΓT, $\mathcal{I} \to 0$ as δN becomes increasingly independent of ϵ. Interestingly, for intermediate ΓT, $\mathcal{I}$ peaks around the peak in χ and close to $T_{\rm SS}$. This demonstrates the correlation between the square-root singularity, $\mathcal{I}$, and the precision. To the best of our knowledge, this is the first demonstration of an information-content enhancement by a square-root singularity, linear or nonlinear. However, the enhancement is only local since much faster scans away from the singularity yield even larger $\mathcal{I}$. Finally, we note that while the exact value of $\mathcal{I}$ depends on the properties of $p_\epsilon(\varepsilon)$, the existence of a peak around $T_{\rm SS}$ (our main result) is independent of those properties as long as $\epsilon \ll \Gamma$ which generally holds in experiments.

Next we assess the effects of averaging. Here, again, our sensor departs from convention. Figures 3(a)-(c) show typical trajectories of the intensity N obtained by averaging n cycles resulting from an identical protocol $F(t)$ and different noise realizations. The circles in Figs. 3(a)-(c) indicate the crossing points, whose difference defines δN. Figures 3(a)-(c) show that, as n increases, the hysteresis widens, δN increases, and trajectories smoothen. Figure 3(d) shows δN versus Δ/Γ for the same three n. Notice the stochastic δN (open data points) approaching the deterministic δN (black solid curve) as n increases. For $n = 500$, the stochastic δN is approximately a square-root function of Δ/Γ for small Δ/Γ. This demonstrates the enhanced sensitivity at the square-root singularity in the presence of noise, albeit only after substantial averaging. Such a time-consuming averaging is of course detrimental for fast sensing. The situation appears to be familiar from conventional linear sensing, where averaging mitigates the effects of noise. However, we show next that the precision of our sensor depends non-trivially on the averaging time.

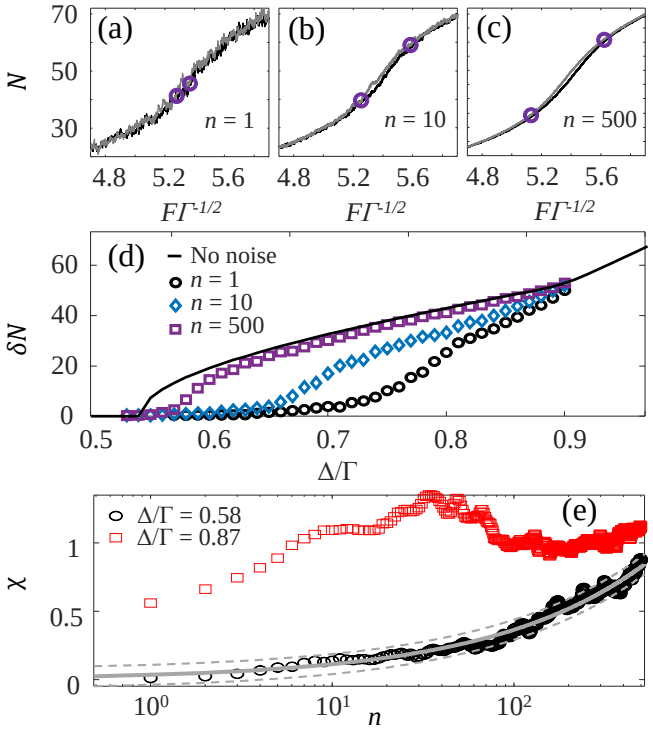

FIG. 3. (a)-(c) N versus $F/\sqrt{\Gamma}$ when scanning $F/\sqrt{\Gamma}$ within $\Gamma T = 10^4$. n is the number of cycles that are averaged. Black (gray) curves are forward (backward) trajectories. Purple circles indicate the crossing points $N_\pm$. (d) Splitting $\delta N = N_+ - N_-$, used as signal for sensing, averaged over n cycles. For reference we show δN when $D = 0$ as a solid black curve. (e) Precision χ versus number of cycles for two different detunings. Solid gray line is a square root fit, with dashed lines indicating 95% confidence bounds. Parameter values are as in Fig. 2 for $\Gamma T = 10^4$. Each curve is an ensemble average of (d) 12 and (e) 120 different noise realizations.

Figure 3(e) shows χ versus n for two distinct Δ/Γ. For each Δ/Γ, we simulated the dynamics of a perturbed ($\epsilon = \Gamma/100$) and an unperturbed cavity. Notice how Δ/Γ affects the dependence of χ on the averaging time. For $\Delta = 0.58\Gamma$, χ increases with the square root of time, as usual in linear sensors. In contrast, for $\Delta = 0.87\Gamma$ (close to Δ_c) χ increases abruptly for $n \lesssim 50$, *decreases* for $50 \lesssim n \lesssim 100$, and then slowly increases for $n \gtrsim 100$. Remarkably, averaging 30 cycles leads to greater precision than averaging 500 cycles. This anomalous behavior is due to the non-trivial dependence of $\mathrm{d}\delta N/\mathrm{d}\Delta$ on n (see SM [60]) near the static square-root singularity. Thus, averaging plays a fundamentally different role in our sensor. Typically, more measurements increase the precision with which an observable is estimated. In contrast, here the precision in ϵ can be increased by restricting the number of measurements.

In summary, we introduced a nonlinear optical sensor where a square-root singularity enhances the sensitivity, precision, and information content of the sig-

nal, and the signal-to-noise ratio increases with the measurement speed. Crucially for applications, our sensing strategy involves simple monochromatic intensity measurements and no error-prone spectral fittings as in EP sensors. Since our sensor involves a single resonator, the cumbersome and slow task of tuning gain or loss is avoided. Instead, the singularity can be accessed dynamically using a commercially-available amplitude modulator to modulate the laser power at the desired speed. All these advantages open up new opportunities for ultrafast and highly-sensitive measurements in noisy environments. Our approach is limited to sufficiently nonlinear resonators displaying hysteresis. While optical hysteresis has been observed in many Kerr-nonlinear resonators [41, 43, 44, 67], some of those systems operate at cryogenic temperatures where sensing applications are limited. An alternative approach could involve thermo-optical nonlinear resonators [46, 49, 52, 68–73], easier to realize at room temperature but limited in speed by thermal dynamics. It remains to be seen whether those sensors can outperform linear sensors. Finally, our approach can be extended to other hysteretic systems, like acoustic [74] or mechanical [75, 76] resonators, MEMS [77, 78], microwave circuits [79], or cavity magnon polaritons [80].

ACKNOWLEDGMENTS

This work is part of the research programme of the Netherlands Organisation for Scientific Research (NWO). We thank Sander Mann, Pieter Rein ten Wolde, and Ewold Verhagen for stimulating discussions. S.R.K.R. acknowledges a NWO Veni grant with file number 016.Veni.189.039.

* s.rodriguez@amolf.nl

[1] J. Wiersig, Enhancing the sensitivity of frequency and energy splitting detection by using exceptional points: application to microcavity sensors for single-particle detection, Phys. Rev. Lett. **112**, 203901 (2014).
[2] C. Dembowski, B. Dietz, H.-D. Gräf, H. L. Harney, A. Heine, W. D. Heiss, and A. Richter, Observation of a chiral state in a microwave cavity, Phys. Rev. Lett. **90**, 034101 (2003).
[3] C. E. Rüter, K. G. Makris, R. El-Ganainy, D. N. Christodoulides, M. Segev, and D. Kip, Observation of parity–time symmetry in optics, Nat. Phys. **6**, 192 (2010).
[4] M. Liertzer, L. Ge, A. Cerjan, A. D. Stone, H. E. Türeci, and S. Rotter, Pump-induced exceptional points in lasers, Phys. Rev. Lett. **108**, 173901 (2012).
[5] B. Peng, Ş. K. Özdemir, S. Rotter, H. Yilmaz, M. Liertzer, F. Monifi, C. M. Bender, F. Nori, and L. Yang, Loss-induced suppression and revival of lasing, Science **346**, 328 (2014).
[6] M. Brandstetter, M. Liertzer, C. Deutsch, P. Klang, J. Schöberl, H. E. Türeci, G. Strasser, K. Unterrainer, and S. Rotter, Reversing the pump dependence of a laser at an exceptional point, Nat. Commun. **5**, 1 (2014).
[7] T. Gao, E. Estrecho, K. Bliokh, T. Liew, M. Fraser, S. Brodbeck, M. Kamp, C. Schneider, S. Höfling, Y. Yamamoto, *et al.*, Observation of non-hermitian degeneracies in a chaotic exciton-polariton billiard, Nature **526**, 554 (2015).
[8] K. Ding, G. Ma, Z. Q. Zhang, and C. T. Chan, Experimental demonstration of an anisotropic exceptional point, Phys. Rev. Lett. **121**, 085702 (2018).
[9] L. Feng, R. El-Ganainy, and L. Ge, Non-hermitian photonics based on parity–time symmetry, Nat. Photon. **11**, 752 (2017).
[10] M.-A. Miri and A. Alù, Exceptional points in optics and photonics, Science **363** (2019).
[11] S. Zhang, Z. Yong, Y. Zhang, and S. He, Parity-time symmetry breaking in coupled nanobeam cavities, Sci. Rep. **6**, 1 (2016).
[12] H. Hodaei, A. U. Hassan, S. Wittek, H. Garcia-Gracia, R. El-Ganainy, D. N. Christodoulides, and M. Khajavikhan, Enhanced sensitivity at higher-order exceptional points, Nature **548**, 187 (2017).
[13] W. Chen, Ş. K. Özdemir, G. Zhao, J. Wiersig, and L. Yang, Exceptional points enhance sensing in an optical microcavity, Nature **548**, 192 (2017).
[14] Z. Xiao, H. Li, T. Kottos, and A. Alù, Enhanced sensing and nondegraded thermal noise performance based on $\mathcal{PT}$-symmetric electronic circuits with a sixth-order exceptional point, Phys. Rev. Lett. **123**, 213901 (2019).
[15] S. R.-K. Rodriguez, Classical and quantum distinctions between weak and strong coupling, Eur. J. Phys. **37**, 025802 (2016).
[16] A. D. McFarland and R. P. Van Duyne, Single silver nanoparticles as real-time optical sensors with zeptomole sensitivity, Nano Lett. **3**, 1057 (2003).
[17] F. Vollmer and S. Arnold, Whispering-gallery-mode biosensing: label-free detection down to single molecules, Nat. Methods **5**, 591 (2008).
[18] J. Zhu, S. K. Ozdemir, Y.-F. Xiao, L. Li, L. He, D.-R. Chen, and L. Yang, On-chip single nanoparticle detection and sizing by mode splitting in an ultrahigh-q microresonator, Nat. Photon. **4**, 46 (2010).
[19] P. Offermans, M. C. Schaafsma, S. R. Rodriguez, Y. Zhang, M. Crego-Calama, S. H. Brongersma, and J. Gómez Rivas, Universal scaling of the figure of merit of plasmonic sensors, ACS Nano **5**, 5151 (2011).
[20] P. Zijlstra, P. M. Paulo, and M. Orrit, Optical detection of single non-absorbing molecules using the surface plasmon resonance of a gold nanorod, Nat. Nanotechnol. **7**, 379 (2012).
[21] M. R. Foreman, J. D. Swaim, and F. Vollmer, Whispering gallery mode sensors, Adv. Opt. Photonics **7**, 168 (2015).
[22] Y. Zhi, X.-C. Yu, Q. Gong, L. Yang, and Y.-F. Xiao, Single nanoparticle detection using optical microcavities, Adv. Mater. **29**, 1604920 (2017).
[23] Z.-P. Liu, J. Zhang, Ş. K. Özdemir, B. Peng, H. Jing, X.-Y. Lü, C.-W. Li, L. Yang, F. Nori, and Y.-x. Liu, Metrology with PT-symmetric cavities: enhanced sensitivity near the PT-phase transition, Phys. Rev. Lett. **117**, 110802 (2016).
[24] J. Wiersig, Sensors operating at exceptional points: general theory, Phys. Rev. A **93**, 033809 (2016).

[25] R. Thomas, H. Li, F. M. Ellis, and T. Kottos, Giant nonreciprocity near exceptional-point degeneracies, Phys. Rev. A **94**, 043829 (2016).

[26] S. Sunada, Large sagnac frequency splitting in a ring resonator operating at an exceptional point, Phys. Rev. A **96**, 033842 (2017).

[27] J. Ren, H. Hodaei, G. Harari, A. U. Hassan, W. Chow, M. Soltani, D. Christodoulides, and M. Khajavikhan, Ultrasensitive micro-scale parity-time-symmetric ring laser gyroscope, Opt. Lett. **42**, 1556 (2017).

[28] A. Hassan, H. Hodaei, W. Hayenga, M. Khajavikhan, and D. Christodoulides, Enhanced sensitivity in parity-time-symmetric microcavity sensors, in *Optical Sensors* (Optical Society of America, 2015) pp. SeT4C–3.

[29] Q. Zhong, J. Ren, M. Khajavikhan, D. N. Christodoulides, Ş. Özdemir, and R. El-Ganainy, Sensing with exceptional surfaces in order to combine sensitivity with robustness, Phys. Rev. Lett. **122**, 153902 (2019).

[30] S. Dong, G. Hu, Q. Wang, Y. Jia, Q. Zhang, G. Cao, J. Wang, S. Chen, D. Fan, W. Jiang, Y. Li, A. Alù, and C.-W. Qiu, Loss-assisted metasurface at an exceptional point, ACS Photonics **7**, 3321 (2020).

[31] C. Yuce and H. Ramezani, Non-diffracting states at exceptional points, Opt. Lett. **46**, 765 (2021).

[32] M. C. Rechtsman, Optical sensing gets exceptional, Nature **548**, 161 (2017).

[33] J. Wiersig, Review of exceptional point-based sensors, Photon. Res. **8**, 1457 (2020).

[34] W. Langbein, No exceptional precision of exceptional-point sensors, Phys. Rev. A **98**, 023805 (2018).

[35] H.-K. Lau and A. A. Clerk, Fundamental limits and non-reciprocal approaches in non-hermitian quantum sensing, Nat. Commun. **9**, 1 (2018).

[36] N. A. Mortensen, P. Gonçalves, M. Khajavikhan, D. N. Christodoulides, C. Tserkezis, and C. Wolff, Fluctuations and noise-limited sensing near the exceptional point of parity-time-symmetric resonator systems, Optica **5**, 1342 (2018).

[37] J. Zhang, B. Peng, Ş. K. Özdemir, K. Pichler, D. O. Krimer, G. Zhao, F. Nori, Y.-x. Liu, S. Rotter, and L. Yang, A phonon laser operating at an exceptional point, Nat. Photon, **12**, 479 (2018).

[38] O. El Daïf, A. Baas, T. Guillet, J.-P. Brantut, R. I. Kaitouni, J. L. Staehli, F. Morier-Genoud, and B. Deveaud, Polariton quantum boxes in semiconductor microcavities, Appl. Phys. Lett. **88**, 061105 (2006).

[39] D. Hunger, T. Steinmetz, Y. Colombe, C. Deutsch, T. W. Hänsch, and J. Reichel, A fiber fabry–perot cavity with high finesse, New J. Phys. **12**, 065038 (2010).

[40] A. A. P. Trichet, J. Foster, N. E. Omori, D. James, P. R. Dolan, G. M. Hughes, C. Vallance, and J. M. Smith, Open-access optical microcavities for lab-on-a-chip refractive index sensing, Lab Chip **14**, 4244 (2014).

[41] H. Abbaspour, S. Trebaol, F. Morier-Genoud, M. T. Portella-Oberli, and B. Deveaud, Stochastic resonance in collective exciton-polariton excitations inside a gaas microcavity, Phys. Rev. Lett. **113**, 057401 (2014).

[42] C. Vallance, A. A. P. Trichet, D. James, P. R. Dolan, and J. M. Smith, Open-access microcavities for chemical sensing, Nanotechnology **27**, 274003 (2016).

[43] S. R. K. Rodriguez, W. Casteels, F. Storme, N. Carlon Zambon, I. Sagnes, L. Le Gratiet, E. Galopin, A. Lemaître, A. Amo, C. Ciuti, and J. Bloch, Probing a dissipative phase transition via dynamical optical hysteresis, Phys. Rev. Lett. **118**, 247402 (2017).

[44] T. Fink, A. Schade, S. Höfling, C. Schneider, and A. Imamoglu, Signatures of a dissipative phase transition in photon correlation measurements, Nat. Phys. **14**, 365 (2018).

[45] M. H. Bitarafan and R. G. DeCorby, On-chip high-finesse fabry-perot microcavities for optical sensing and quantum information, Sensors **17** (2017).

[46] Z. Geng, K. J. H. Peters, A. A. P. Trichet, K. Malmir, R. Kolkowski, J. M. Smith, and S. R. K. Rodriguez, Universal scaling in the dynamic hysteresis, and non-Markovian dynamics, of a tunable optical cavity, Phys. Rev. Lett. **124**, 153603 (2020).

[47] K. J. H. Peters, Z. Geng, K. Malmir, J. M. Smith, and S. R. K. Rodriguez, Extremely broadband stochastic resonance of light and enhanced energy harvesting enabled by memory effects in the nonlinear response, Phys. Rev. Lett. **126**, 213901 (2021).

[48] L. Shao, X.-F. Jiang, X.-C. Yu, B.-B. Li, W. R. Clements, F. Vollmer, W. Wang, Y.-F. Xiao, and Q. Gong, Detection of single nanoparticles and lentiviruses using microcavity resonance broadening, Adv. Mater. **25**, 5616 (2013).

[49] V. R. Almeida and M. Lipson, Optical bistability on a silicon chip, Opt. Lett. **29**, 2387 (2004).

[50] A. Ksendzov and Y. Lin, Integrated optics ring-resonator sensors for protein detection, Opt. Lett. **30**, 3344 (2005).

[51] Y. Zuta, I. Goykhman, B. Desiatov, and U. Levy, On-chip switching of a silicon nitride micro-ring resonator based on digital microfluidics platform, Opt. Express **18**, 24762 (2010).

[52] M. Notomi, A. Shinya, S. Mitsugi, G. Kira, E. Kuramochi, and T. Tanabe, Optical bistable switching action of Si high-Q photonic-crystal nanocavities, Opt. Express **13**, 2678 (2005).

[53] Y. Liu and H. W. M. Salemink, Photonic crystal-based all-optical on-chip sensor, Opt. Express **20**, 19912 (2012).

[54] D. Threm, Y. Nazirizadeh, and M. Gerken, Photonic crystal biosensors towards on-chip integration, J. Biophotonics **5**, 601 (2012).

[55] D.-Q. Yang, B. Duan, X. Liu, A.-Q. Wang, X.-G. Li, and Y.-F. Ji, Photonic crystal nanobeam cavities for nanoscale optical sensing: A review, Micromachines **11** (2020).

[56] K. Perrier, S. Greveling, H. Wouters, S. R. K. Rodriguez, G. Lehoucq, S. Combrié, A. de Rossi, S. Faez, and A. P. Mosk, Thermo-optical dynamics of a nonlinear gainp photonic crystal nanocavity depend on the optical mode profile, OSA Continuum **3**, 1879 (2020).

[57] B. Garbin, A. Giraldo, K. J. H. Peters, N. G. R. Broderick, A. Spakman, F. Raineri, A. Levenson, S. R. K. Rodriguez, B. Krauskopf, and A. M. Yacomotti, Spontaneous symmetry breaking in a coherently driven nanophotonic bose-hubbard dimer, Phys. Rev. Lett. **128**, 053901 (2022).

[58] I. Carusotto and C. Ciuti, Quantum fluids of light, Rev. Mod. Phys. **85**, 299 (2013).

[59] F. Broner, G. H. Goldsztein, and S. H. Strogatz, Dynamical hysteresis without static hysteresis: Scaling laws and asymptotic expansions, SIAM J. Appl. Math. **57**, 1163 (1997).

[60] See Supplemental Material [url] for details about the role of model parameters, the maximum attainable sensitivity versus the driving speed, how the sensitivity scales with the number of cycles, a comparison of our nonlinear sensor to a linear sensor, and an analysis of detuning noise which refers to Ref. 61.

[61] D. T. Gillespie, The mathematics of Brownian motion and Johnson noise, Am. J. Phys. **64**, 225 (1996).

[62] S. Kiesewetter, R. Polkinghorne, B. Opanchuk, and P. D. Drummond, xSPDE: Extensible software for stochastic equations, SoftwareX **5**, 12 (2016).

[63] M. Zhang, W. Sweeney, C. W. Hsu, L. Yang, A. D. Stone, and L. Jiang, Quantum noise theory of exceptional point amplifying sensors, Phys. Rev. Lett. **123**, 180501 (2019).

[64] P. Jung, G. Gray, R. Roy, and P. Mandel, Scaling law for dynamical hysteresis, Phys. Rev. Lett. **65**, 1873 (1990).

[65] S. M. Kay, Fundamentals of statistical signal processing. detection theory, volume ii, Printice Hall PTR , 1545 (1998).

[66] T. M. Cover and J. A. Thomas, Entropy, relative entropy and mutual information, in *Elements of information theory* (1991).

[67] L. Pickup, K. Kalinin, A. Askitopoulos, Z. Hatzopoulos, P. G. Savvidis, N. G. Berloff, and P. G. Lagoudakis, Optical bistability under nonresonant excitation in spinor polariton condensates, Phys. Rev. Lett. **120**, 225301 (2018).

[68] T. Carmon, L. Yang, and K. J. Vahala, Dynamical thermal behavior and thermal self-stability of microcavities, Opt. Express **12**, 4742 (2004).

[69] G. Priem, P. Dumon, W. Bogaerts, D. V. Thourhout, G. Morthier, and R. Baets, Optical bistability and pulsating behaviour in silicon-on-insulator ring resonator structures., Opt. Express **13**, 9623 (2005).

[70] Y. Shi, X. Chen, F. Lou, Y. Chen, M. Yan, L. Wosinski, and M. Qiu, All-optical switching of silicon disk resonator based on photothermal effect in metal-insulator-metal absorber, Opt. Lett. **39**, 4431 (2014).

[71] M. Brunstein, R. Braive, R. Hostein, A. Beveratos, I. Robert-Philip, I. Sagnes, T. J. Karle, A. M. Yacomotti, J. A. Levenson, V. Moreau, G. Tessier, and Y. D. Wilde, Thermo-optical dynamics in an optically pumped photonic crystal nano-cavity, Opt. Express **17**, 17118 (2009).

[72] M. Sodagar, M. Miri, A. A. Eftekhar, and A. Adibi, Optical bistability in a one-dimensional photonic crystal resonator using a reverse-biased pn-junction, Opt. Express **23**, 2676 (2015).

[73] K. J. H. Peters, Z. Geng, K. Malmir, J. M. Smith, and S. R. K. Rodriguez, Extremely broadband stochastic resonance of light and enhanced energy harvesting enabled by memory effects in the nonlinear response, Phys. Rev. Lett. **126**, 213901 (2021).

[74] G. Lyakhov, A. Proskuryakov, K. Shipilov, and O. Umnova, Bistability and chaos in acoustic resonators, Ultrasonics **33**, 55 (1995).

[75] L. Papariello, O. Zilberberg, A. Eichler, and R. Chitra, Ultrasensitive hysteretic force sensing with parametric nonlinear oscillators, Phys. Rev. E **94**, 022201 (2016).

[76] A. Chowdhury, S. Barbay, M. G. Clerc, I. Robert-Philip, and R. Braive, Phase stochastic resonance in a forced nanoelectromechanical membrane, Phys. Rev. Lett. **119**, 234101 (2017).

[77] W. Zhang, R. Baskaran, and K. L. Turner, Effect of cubic nonlinearity on auto-parametrically amplified resonant MEMS mass sensor, Sens. Actuator. A Phys. **102**, 139 (2002).

[78] M. H Hasan, A. Abbasalipour, H. Nikfarjam, S. Pourkamali, M. Emad-Un-Din, R. Jafari, and F. Alsaleem, Exploiting pull-in/pull-out hysteresis in electrostatic MEMS sensor networks to realize a novel sensing continuous-time recurrent neural network, Micromachines **12**, 268 (2021).

[79] D. L. Sounas, J. Soric, and A. Alu, Broadband passive isolators based on coupled nonlinear resonances, Nat. Electron. **1**, 113 (2018).

[80] Y.-P. Wang, G.-Q. Zhang, D. Zhang, T.-F. Li, C.-M. Hu, and J. Q. You, Bistability of cavity magnon polaritons, Phys. Rev. Lett. **120**, 057202 (2018).